Journal of Colloid and Interface Science 702 (2026) 138801

Contents lists available at ScienceDirect

Journal of Colloid And Interface Science

journal homepage: www.elsevier.com/locate/jcis

Ozone-coupled photocatalytic H_2O_2 synthesis via Mn/Ce bimetallic metal organic framework: synergistic catalysis and sacrificial agent-free efficiency

Guanqing Song [a,b,1], Chi Song [b,1], Gansheng Shi [b], Xiao Wang [b,c], Guanhong Lu [b], Lu Chen [b], Jing Sun [b,c], Xiaofeng Xie [b,*]

[a] Jiangsu Key Laboratory of Coal-based Greenhouse Gas Control and Utilization, China University of Mining and Technology, 221008 Xuzhou, Jiangsu, China
[b] Shanghai Institute of Ceramics, Chinese Academy of Sciences, Shanghai 200050, China
[c] University of Chinese Academy of Sciences, 19 (A) Yuquan Road, Beijing 100049, China

HIGHLIGHTS

- First demonstration of O_3 activation via Mn(II)/Ce(III) synergy, generating Mn (III)-*OOOH intermediates.
- Ce-doping reduces the rate-determining step energy barrier by 89 % through optimized Mn-O-Ce charge transfer.
- Sustained catalytic cycling with 83 % charge utilization efficiency.
- Eliminates sacrificial agents while utilizing industrially scalable O_3 sources.

GRAPHICAL ABSTRACT

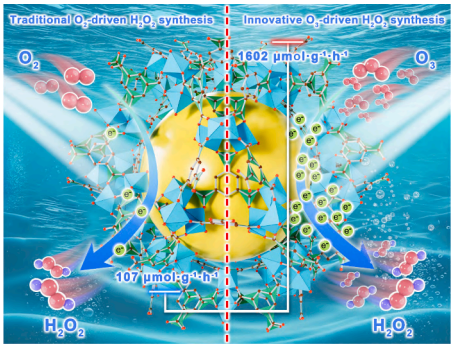

ARTICLE INFO

Keywords:
Ozone
MIL-100
Photocatalytic
Hydrogen peroxide
Synthesis

ABSTRACT

Typically, photocatalytic H_2O_2 synthesis faces efficiency limitations due to sacrificial agent dependence and sluggish oxygen activation. Herein, we present, for the first time, an ozone-coupled bimetallic MIL-100(Mn_1Ce_2) photocatalytic approach to H_2O_2 synthesis. This novel strategy yields an impressive 1602 $\mu mol \cdot g^{-1} \cdot h^{-1}$ H_2O_2 in pure water without sacrificial agents. This represents a 240 % boost in efficiency compared to its single-metallic analogs (MIL-100(Mn)), while maintaining exceptional stability for over 50 h. Comprehensive mechanistic investigations elucidate a pioneering reaction pathway: Mn(II) activates O_3, producing Mn(III)-*OOOH intermediates. Meanwhile, Ce doping effectively reduces the energy barrier of the rate-determining step from 0.37 eV to 0.04 eV by optimizing the Mn-O-Ce charge-transfer route. Moreover, the continuous generation of photoelectrons ensures the regeneration of Mn(III) to Mn(II), maintaining a catalytic cycle with a charge utilization efficiency of 83 %. This study establishes a platform for O_3-Metal Organic Framework co-operation, an innovative breakthrough from the traditional limitations of solar-driven H_2O_2 synthesis.

* Corresponding author at: Jiangsu Key Laboratory of Coal-based Greenhouse Gas Control and Utilization and Shanghai Institute of Ceramics, Chinese Academy of Science, China.
E-mail address: xxfshcn@163.com (X. Xie).
[1] Co-first authors.

https://doi.org/10.1016/j.jcis.2025.138801
Received 30 May 2025; Received in revised form 20 August 2025; Accepted 21 August 2025
Available online 22 August 2025

1. Introduction

One of the global hotspots for sustainable energy research is the low-carbon, efficient, and clean manufacturing of high-value energy carrier compounds. Hydrogen peroxide (H_2O_2) is an eco-friendly oxidant and a promising clean fuel with applications ranging from medical disinfection to water treatment and chemical synthesis [1–3]. The market value of H_2O_2 is predicted to reach $15.4 billion by 2030 [4], but conventional processes based on anthraquinone remain energy-intensive, solvent-dependent, and environmentally hazardous [5].

Solar-driven photocatalytic H_2O_2 synthesis is a promising sustainable technology [6–8], yet traditional O_2-based systems face intrinsic limitations: (1) poor O_2 solubility (8.26 mg/L at 25 °C) results in sluggish reaction kinetics [9]; (2) low O_2 reactivity and competing four-electron oxygen reduction reaction (ORR) limit H_2O_2 yield [10] and (3) inefficient electron-hole separation frequently necessitating the use of sacrificial agents as mediators [11]. To transcend these limitations, exploring more reactive gaseous sources is crucial for enhancing H_2O_2 production efficiency.

Ozone (O_3), a highly reactive oxygen allotrope, offers strong oxidative capacity, high selectivity, and fast reaction kinetics, making it valuable in photocatalysis [12]. Compared to O_2, O_3 has higher solubility (570 mg/L, 25 °C) and superior reactivity in aqueous environments [13]. During ozone decomposition, O_3 generates highly reactive oxygen radicals (e.g., *O, *OO, and •OH), facilitating the production of H_2O_2 [14]. Additionally, O_3 can be produced on an industrial scale through established and cost-effective methods, such as electrochemical and dielectric-barrier discharges [15], rendering O_3 a practical alternative for large-scale applications.

Building on our previous work with Mn/Ln-BTC frameworks [16], which highlighted the synergy between manganese and rare-earth elements in promoting ozone conversion. In this work, we have developed a novel ozone-assisted photocatalytic strategy by engineering a bimetallic MIL-100(Mn_1Ce_2) framework via a post-synthetic approach (Schematic 1). This design exploits the high reactivity and solubility of O_3 to bypass the inherent limitations of O_2. The cooperative Mn/Ce interactions lower the activation barrier and enable continuous catalytic cycling, establishing a new paradigm for solar-driven H_2O_2 synthesis. Our findings demonstrate a significant advancement in photocatalytic H_2O_2 production and set the stage for further breakthroughs in sustainable energy conversion and green chemical manufacturing.

2. Experimental

2.1. Materials

Trimesic Acid (99 %+), Manganese(II) Nitrate Tetrahydrate (Mn$(NO_3)_2{\cdot}4H_2O$), and Cerium (III) nitrate hexahydrate ($Ce(NO_3)_3{\cdot}6H_2O$) were obtained from Shanghai Titan Scientific Co., Ltd. Ethanol and methanol were purchased from Shanghai Zhenxing Co., Ltd., and Shanghai Lingfeng chemical reagent Co., Ltd., respectively. The materials mentioned above were used without any prior purification.

2.2. Catalyst synthesis

MIL-100(Mn) and MIL-100(Ce) were prepared by a modified solvothermal method [17]. Bimetallic frameworks of MIL-100(Mn_1/Ce_2) were prepared via: (i) in situ one-pot synthesis (MIL-100(Mn_1Ce_2)-i) or (ii) post-synthetic Ce incorporation into MIL-100(Mn) (MIL-100(Mn_1Ce_2)-p).

Synthesis of MIL-100(Mn): 6 mmol $Mn(NO_3)_2{\cdot}4H_2O$ was dissolved in methanol, and then H_3BTC was added with continuous stirring until a

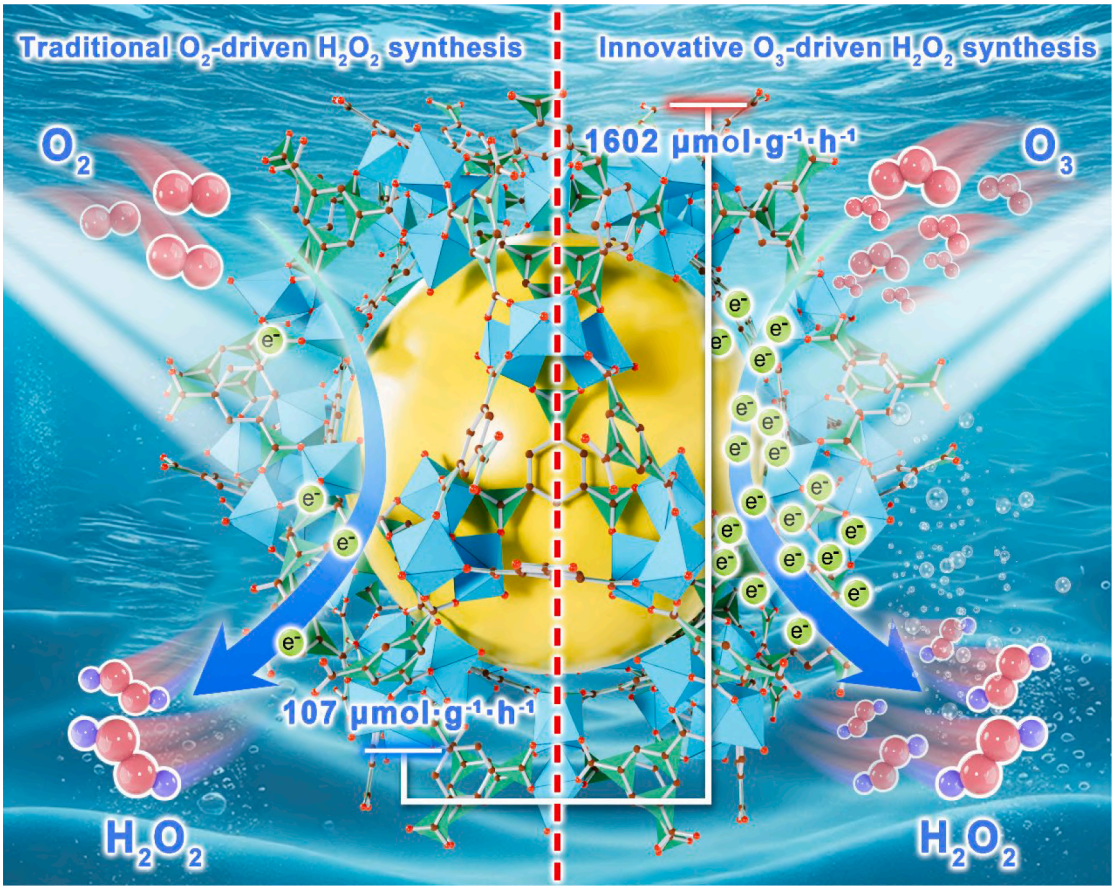

Schematic 1. Ozone-assisted photocatalytic synthesis of H_2O_2.

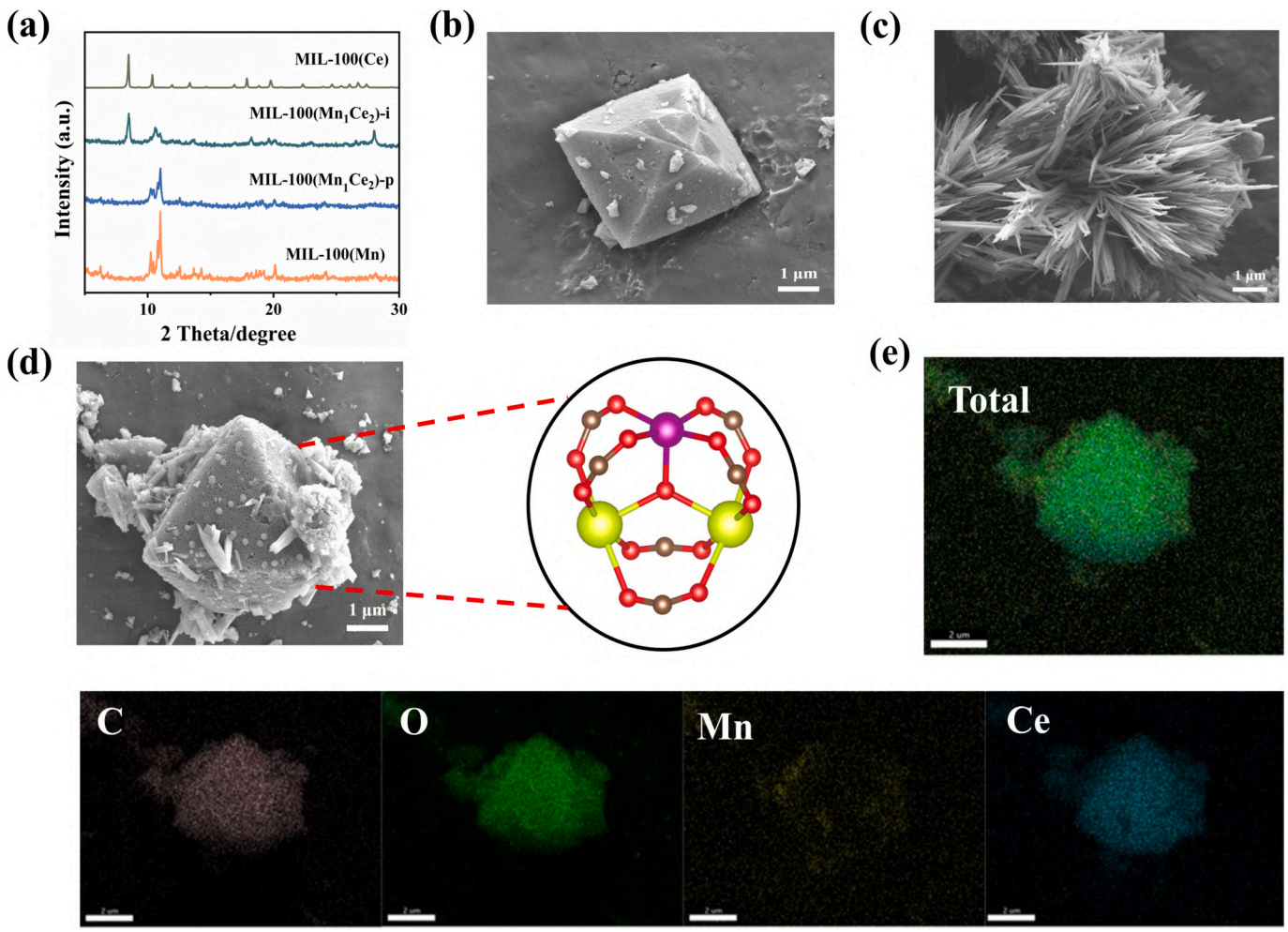

Fig. 1. **(a)** Powder X-ray diffraction patterns of the obtained samples, **(b-d)** Scanning electron micrographs of MIL-100(Mn), MIL-100(Ce), and post-synthetic MIL-100(Mn_1Ce_2)-p, respectively, **(e)** EDS elemental distribution map for MIL-100(Mn_1Ce_2)-p.

transparent solution was obtained. Subsequently, the attained mixture was fed into an autoclave and heated at 120 °C for 3 h. Then, the samples were washed three times with ethanol and dried under a vacuum overnight to obtain MIL-100(Mn).

Synthesis of MIL-100(Ce): 6 mmol $Ce(NO_3)_3{\cdot}6H_2O$ was dissolved in methanol, and then H_3BTC was added with continuous stirring until a transparent solution was obtained. Subsequently, the attained mixture was fed into an autoclave and heated at 120 °C for 3 h. Then, the samples were washed three times with ethanol and dried under a vacuum overnight to obtain MIL-100(Ce).

Synthesis of MIL-100(Mn_1Ce_2)-i: 2 mmol $Mn(NO_3)_2{\cdot}4H_2O$ and 4 mmol $Ce(NO_3)_3{\cdot}6H_2O$ were dissolved in methanol, then H_3BTC was added with continuous stirring until a transparent solution was obtained. Subsequently, the attained mixture was fed into an autoclave and heated at 120 °C for 3 h. Then, the samples were washed three times with ethanol and dried under a vacuum overnight to obtain MIL-100(Mn_1Ce_2)-i.

Synthesis of MIL-100(Mn_1Ce_2)-p: The above-obtained MIL-100(Mn) was redispersed into a methanol solution, followed by the addition of 4 mmol of $Ce(NO_3)_3{\cdot}6H_2O$. After thoroughly stirring the mixed solution, it was fed into an autoclave and heated at 120 °C for 3 h. Then, the samples were washed three times with ethanol and dried under a vacuum overnight to obtain MIL-100(Mn_1/Ce_2)-p.

2.3. Materials characterization

Crystal structure information is acquired by a power X-ray diffractometer (D8 ADVANCE). The microstructure and EDS mapping of the materials were obtained through a scanning electron microscope (Hitachi SU8220). The X-ray photoelectron spectrometer (ESCAlab250, USA) captured the elemental valence state and coordination environment. Cary 5000 UV–Vis-NIR was conducted to analyze the samples' UV–vis absorption spectra. The photoluminescence (PL) spectroscopy was tested on a PerkinElmer Inc. - LS 55 Luminescence Spectrometer with a wavelength of 420 nm. The transient photocurrent experiment was undertaken by a CHI660D photoelectrochemical workstation equipped with a three-electrode system. The degradation curve of ozone was collected by an ozone Analyzer (Model 49i, U.S.A. EPA).

2.4. Photocatalytic H_2O_2 production

2.4.1. Photocatalytic reaction

In a typical experiment, the photosynthesis of H_2O_2 was performed in a 100 mL quartz beaker containing 5 mg photocatalyst, and 45 mL deionized water was sonicated in the dark for 30 min and ozone bubbles for 10 min. Then, the system was irradiated with a 300 W xenon lamp (CEL-LAX, China). After 5 h of illumination, filter the catalyst and detect the H_2O_2 content in the solution.

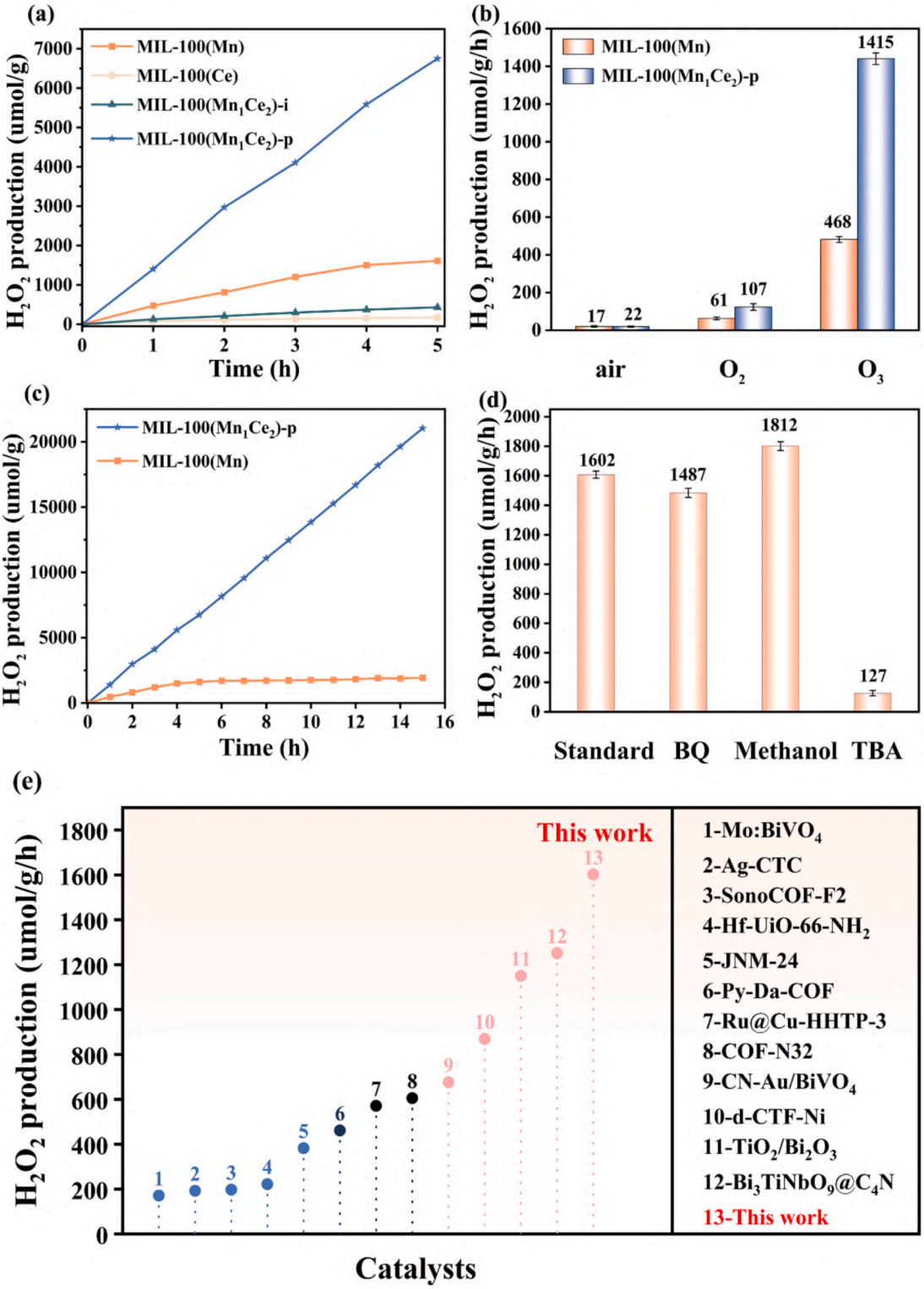

Fig. 2. **(a)** Time course of photocatalytic H_2O_2 production for different samples using a 300 W xenon lamp equipped with a filter ($\lambda > 420$ nm), **(b)** Performance testing of MIL-100(Mn) and MIL-100(Mn_1Ce_2)-p in different atmospheres, **(c)** Long-term photocatalytic H_2O_2 production of MIL-100(Mn) and MIL-100(Mn_1Ce_2)-p, **(d)** Cyclic test curve for MIL-100(Mn_1Ce_2)-p and **(e)** Comparison of the H_2O_2 production efficiency with other representative photocatalysts.

2.4.2. *H_2O_2 detection method*

The amount of H_2O_2 was analyzed by Iodometry. After 5 h of light reaction, add an appropriate amount of the solution filtered through a 0.22 μm filter membrane into a 10 mL volumetric flask and dilute with water. Remove 2 mL of solution and add 1 mL of 0.1 M aqueous potassium hydrogen phthalate ($C_8H_5KO_4$) and 1 mL of 0.4 M aqueous potassium iodide (KI) to the remaining solution. The absorbance of the signal peak around 350 nm was measured by an ultraviolet spectrophotometer and brought into the standard curve formula to calculate the production of H_2O_2. (Fig. S1).

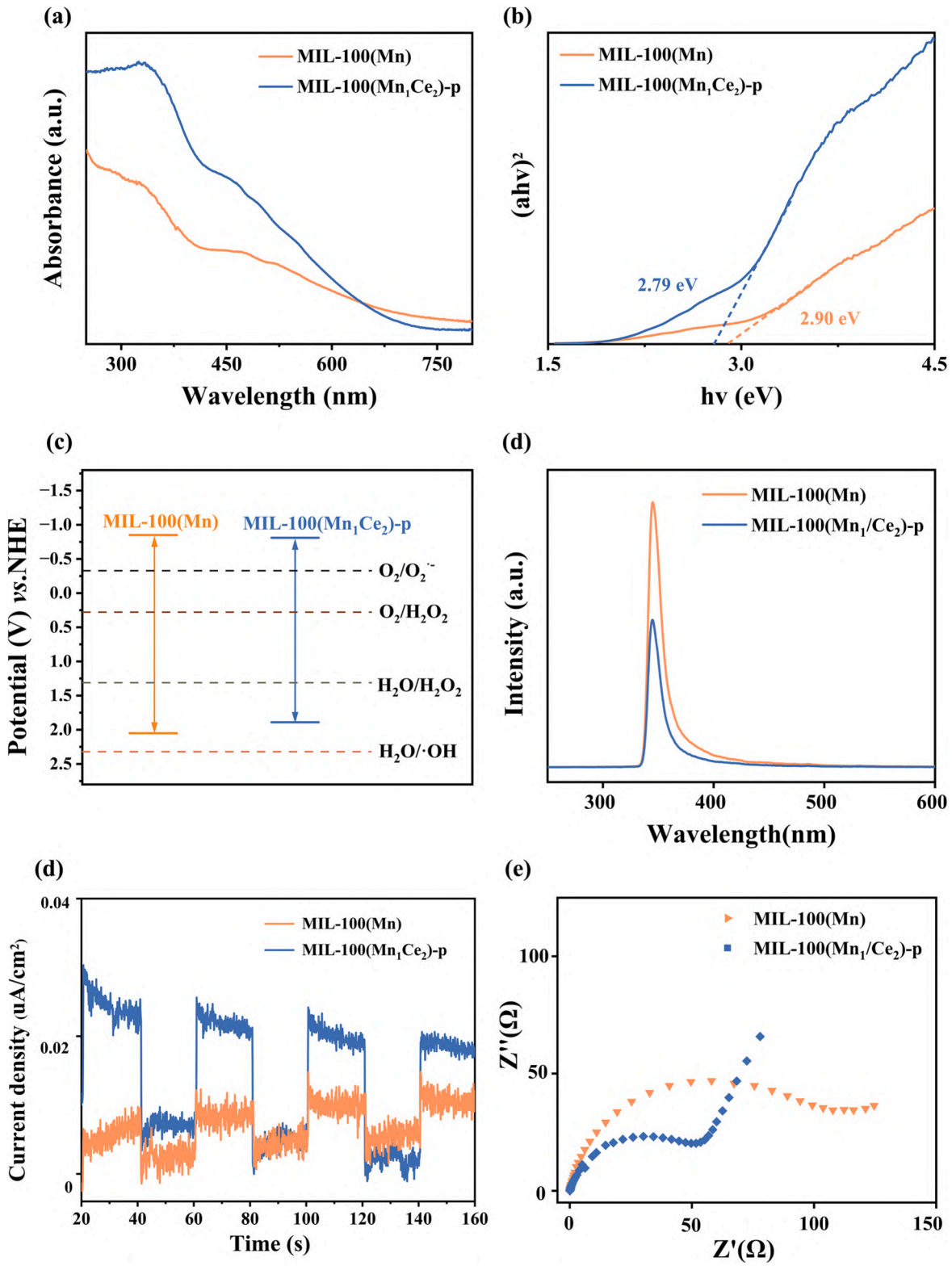

Fig. 3. The optical and electronic properties of MIL-100(Mn) and MIL-100(Mn_1Ce_2) **(a)** UV–vis spectra, **(b)** The converted Kubelka-Munk function curve, **(c)** Band structure diagrams, **(d)** Photoluminescence spectra, **(e)** Transient photocurrent responses, and **(f)** Nyquist plots.

2.5. DFT calculations

Our spin-polarized density functional theory (DFT) calculations were executed with the CP2K code. For computational feasibility, the MIL-100 cluster models were constructed to investigate the behavior of O_3. As shown in Fig. S2, the MIL-100 cluster model with 124 atoms contains the Mn/Er metal node with six benzoate ligands. The Brillouin-zone integration was sampled with a Γ-centered Monkhorst-Pack mesh of 1 × 1 × 1.

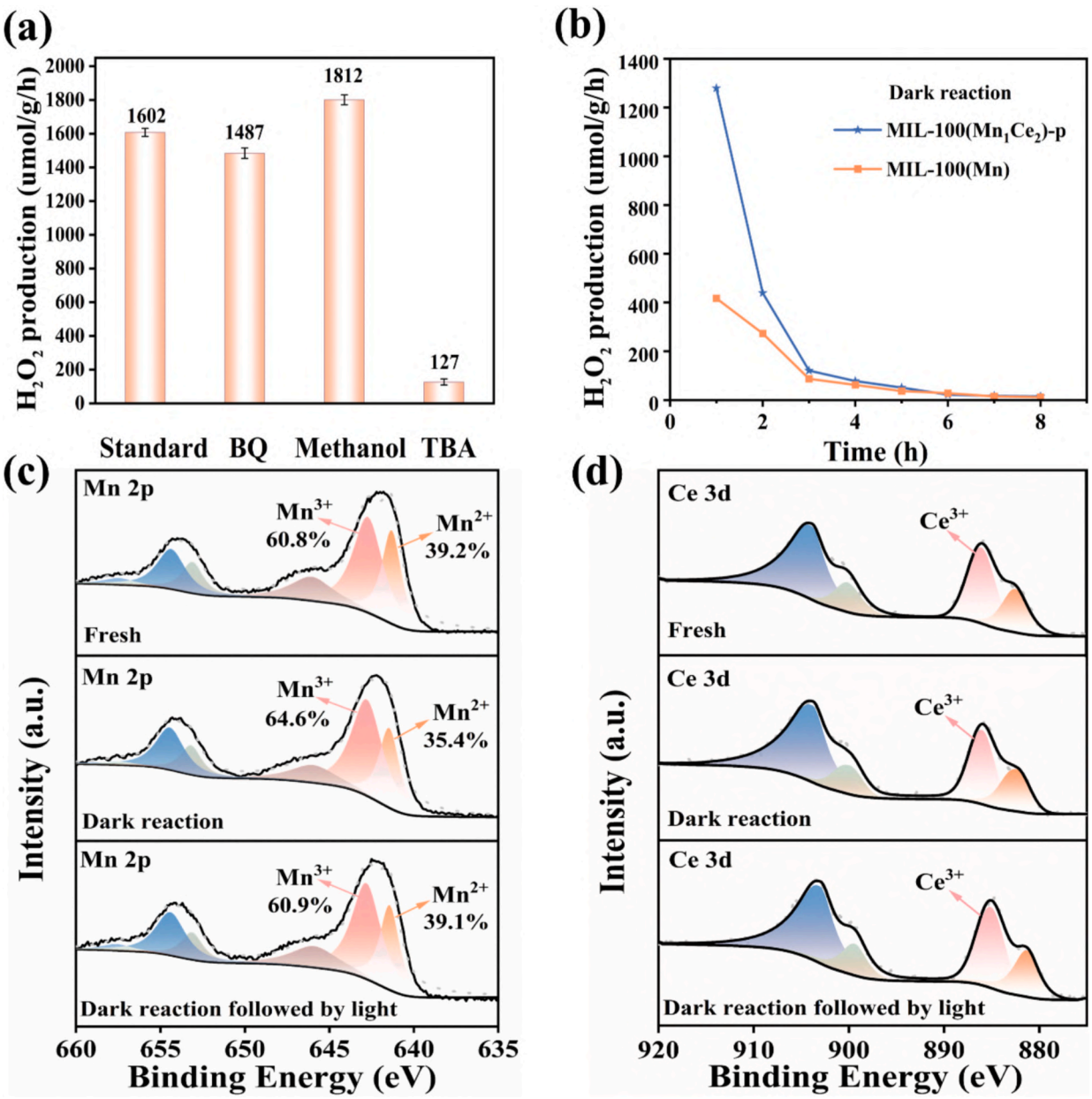

Fig. 4. **(a)** Photocatalytic H_2O_2 production activities of MIL-100(Mn_1Ce_2) with the addition of different sacrificial agents, **(b)** H_2O_2 production rate of MIL-100 (Mn_1Ce_2) under dark reaction conditions, in situ XPS mapping of MIL-100(Mn_1Ce_2) **(c)** Mn 2p, **(d)** Ce 3d.

3. Results and discussion

3.1. Synthesis and structural characterization

As illustrated in Fig. 1, X-ray diffraction and scanning electron microscopy verify that MIL-100(Mn) retains the archetypal octahedral framework, whereas MIL-100(Ce) adopts a rod-like, stacked morphology characteristic of the Ln-BTC topology [18]. Pang et al. [19] demonstrated that Ce coordinates with BTC^{3-} considerably faster than Mn in methanol, complicating the uniform incorporation of rare-earth ions into MIL-100(Mn) via a one-pot method. Our experiment corroborates this observation: MIL-100(Mn_1Ce_2)-i adopts a Janus morphology [20] (Fig. S3), and ICP-OES analysis (Table S1) reveals a Ce: Mn ratio of 4.08:1, deviating from the ideal 2:1. Notably, MIL-100(Mn_1Ce_2)-p retains the crystalline structure of archetypal octahedral (Fig. 1d), and ICP-OES analysis yielded a Ce/Mn ratio of 2.05:1 (Table S1), closely aligning with the ideal 2:1 ratio. Moreover, energy-dispersive X-ray spectroscopy confirms homogeneous Ce distribution (Fig. 1e), underscoring the feasibility of the post-synthetic strategy.

Nitrogen adsorption-desorption measurements were conducted to evaluate the catalysts' porosity and specific surface area. As depicted in Fig. S4, the N_2 adsorption-desorption isotherms of MIL-100(Ce) and MIL-100(Mn_1Ce_2)-i exhibit characteristic type III behavior, whereas MIL-100(Mn) and MIL-100(Mn_1Ce_2)-p follow type I sorption isotherms. The BET surface areas of MIL-100(Mn), MIL-100(Ce), MIL-100 (Mn_1Ce_2)-i, and MIL-100(Mn_1Ce_2)-p were measured as 892, 37, 43, and 560 m^2/g, respectively. These results substantiate the efficacy of the post-synthetic strategy.

3.2. Photosynthesis H_2O_2 production

The visible-light photosynthesis of H_2O_2 was investigated in pure water under an O_3 atmosphere, with yields quantified via iodometric titration [21]. The H_2O_2 production rates were measured using different

photocatalysts in 45 mL of water. MIL-100(Mn_1Ce_2)-p furnished the highest H_2O_2 production rate of 1403 μmol·g^{-1}·h^{-1}, with a linear increase over 5 h. In contrast, MIL-100(Mn) reached 474 μmol·g^{-1}·h^{-1} but showed a significant deceleration after 4 h, while MIL-100(Ce) and MIL-100(Mn_1Ce_2)-i achieved much lower rates of 78 and 127 μmol·g^{-1}·h^{-1}, respectively (Fig. 2a). Accordingly, further discussion focuses on MIL-100(Mn) and MIL-100(Mn_1Ce_2)-p.

The reaction atmosphere is crucial for H_2O_2 production. In a pure ozone environment, the yield was 6.7 times higher than under O_2, while negligible H_2O_2 was detected with continuous airflow, underscoring the necessity of O_3 (Fig. 2b). The effect of O_3 concentration was further examined (Fig. S5), with MIL-100(Mn_1Ce_2)-p achieving an optimal production efficiency of 1602 μmol·g^{-1}·h^{-1} at 700 ppb. Beyond this concentration threshold (>700 ppb), a marked decline in production rate is observed, likely due to the decomposition of the generated H_2O_2 by residual ozone. Photostability and recyclability were assessed to evaluate catalyst durability. MIL-100(Mn) plateaued after 6 h, whereas MIL-100(Mn_1Ce_2)-p showed a continuous linear increase over 15 h, yielding 21,035 μmol H_2O_2 (Fig. 2c). Cycling experiments demonstrated that MIL-100(Mn_1Ce_2)-p retained 91 % of its initial activity after five 10-h cycles, confirming its exceptional stability (Fig. 2d). A comparison with other reported catalysts is provided in Fig. 2e and Table S3 [22–33], MIL-100(Mn_1Ce_2)-p outperforms the majority of reported catalysts, underscoring its promising potential for large-scale H_2O_2 production in pure water.

3.3. Optics and electrochemistry

Ultraviolet-visible (UV–Vis) spectroscopy (Fig. 3a) reveals that both MIL-100(Mn) and MIL-100(Mn_1Ce_2)-p exhibit light absorption within the visible spectrum (400–800 nm). The band gaps (Eg) of MIL-100(Mn) and MIL-100(Mn_1Ce_2)-p are determined to be 2.90 and 2.79 eV by Tauc plots (Fig. 3b). Mott–Schottky measurements (Fig. S6) yield conduction band (CB) potentials of −0.85 eV for MIL-100(Mn) and − 0.81 eV for MIL-100(Mn_1Ce_2)-p. The band structure is obtained by the equation $Eg = E_C - E_V$. Given the reduction potentials of $O_2(g)/O_2^{\cdot-}$ (−0.35 V), $O_2(g)/H_2O_2$ (0.28 V), and the oxidation potential of H_2O/H_2O_2 (1.35 V vs. NHE at pH 7), both MIL-100(Mn) and MIL-100(Mn_1Ce_2)-p are thermodynamically suitable for the Oxygen Reduction Reaction (ORR) and Water Oxidation Reaction (WOR).

Photoluminescence (PL) spectroscopy, electrochemical impedance spectroscopy (EIS), and transient photocurrent tests were conducted to investigate the optical and photoelectrochemical properties of MIL-100 (Mn) and MIL-100(Mn_1Ce_2)-p. Steady-state PL spectra (Fig. 3d) show significantly lower emission intensity for MIL-100(Mn_1Ce_2)-p, indicating enhanced photoinduced electron-hole separation and efficient electron transfer. Additionally, its higher photocurrent density (Fig. 3e) confirms improved charge carrier separation. EIS spectra (Fig. 3f) reveal semicircular Nyquist plots for both materials, with MIL-100(Mn_1Ce_2)-p exhibiting lower charge transfer resistance, further highlighting its superior charge separation efficiency.

3.4. Investigation of the reaction mechanism

A series of control experiments was performed to elucidate the photocatalytic mechanism. To assess the contribution of O_3 alone, reactions were conducted under an O_3 atmosphere without catalysts (Fig. S7). The results corroborate that O_3 can generate H_2O_2, consistent with previous reports [14,34]. However, the average H_2O_2 production rate over 5 h was only 13 μmol·g^{-1}·h^{-1}, indicating a negligible contribution to the overall H_2O_2 formation in this system.

In photocatalytic H_2O_2 production, Oxygen Reduction Reaction (ORR) and Water Oxidation Reaction (WOR) are typically involved. Although the band gaps of MIL-100(Mn) and MIL-100(Mn_1Ce_2)-p suggest the potential generation of H_2O_2 via the ORR pathway, the efficiency of H_2O_2 production under O_2 is only 7.5 % of that observed under O_3 (Fig. 2a). To assess the contribution of the ORR pathway, p-benzoquinone (BQ) was introduced as a $\cdot O_2^-$ scavenger, which led to a partial suppression of H_2O_2 formation (Fig. 4a). This result indicates the presence of an ORR pathway in the system, albeit with a relatively limited contribution. Photo-generated holes play a key role in the WOR process. Interestingly, introducing methanol as a hole scavenger unexpectedly enhanced the H_2O_2 yield rather than decreasing it, suggesting that O_3 promotes H_2O_2 formation through a distinct mechanism.

Previous studies [35,36] have demonstrated that O_3 decomposition generates hydroperoxyl radicals (*OOOH), which spontaneously dissociate into O_2 and hydroxyl radicals (•OH) in aqueous media. The recombination of the •OH species forms H_2O_2. Adding tert-butanol (TBA) as a hydroxyl radical (•OH) scavenger has been performed, showing a rapid decline in H_2O_2 production to 127 μmol·g^{-1}·h^{-1}, which corroborates the proposed reaction pathway.

Ozone exposure typically increases the oxidation state of metal catalysts, a process that occurs independently of light. Experiments were conducted under dark conditions to elucidate the mechanism of H_2O_2 generation. MIL-100(Mn) exhibited an initial H_2O_2 generation rate of 417 μmol·g^{-1}·h^{-1} in the first hour, comparable to that observed under illumination. However, its efficiency declined sharply after 2 h and nearly ceased after 5 h. A similar trend was observed for MIL-100 (Mn_1Ce_2), which initially achieved 1279 μmol·g^{-1}·h^{-1} but underwent a rapid decrease beyond 2 h. This behavior suggests that low-valence metal sites (e.g., Mn^{2+}, Ce^{3+}) act as active centers, while their oxidation by O_3 (e.g., Mn^{3+}, Ce^{4+}) deactivates the catalyst, suppressing further H_2O_2 generation. Notably, when pre-reacted samples were subsequently exposed to light, H_2O_2 production resumed. While MIL-100(Mn) exhibited a slight decline after 5 h of illumination, MIL-100 (Mn_1Ce_2) sustained an almost linear increase in H_2O_2 yield over the same period.

X-ray photoelectron spectroscopy (XPS) was conducted to investigate the oxidation states of manganese and cerium. High-resolution XPS spectra (Fig. 4c) reveal Mn peaks at 641.4 eV and 642.8 eV, which can be assigned to Mn^{2+} and Mn^{3+}, respectively [37]. Following the dark reaction, the Mn^{2+} fraction decreased from 39.2 % to 35.4 %, while subsequent light irradiation restored it to 39.1 %, supporting the proposed reaction pathway. The Ce^{3+} signal was identified at 886.17 eV, whereas the characteristic Ce^{4+} peak at 916.0 eV [38] was absent throughout the in-situ reaction (Fig. 4d), indicating that cerium remained in the trivalent state. These findings suggest that in MIL-100(Mn_1Ce_2), Mn serves as the active center for O_3 degradation, while Ce acts as structural support, modulating the electronic distribution. For comparison, the in situ XPS analysis of MIL-100(Mn) (Fig. S8) revealed a decrease in Mn^{2+} from 39.2 % to 27.0 % during the dark reaction, with partial recovery to 31.4 % upon light exposure. This behavior is attributed to the limited photogenerated electron utilization in MIL-100(Mn), where only a small fraction of Mn^{3+} is reduced back to Mn^{2+} via photoreduction.

Based on the above results, we propose a reaction pathway for O_3-assisted photocatalytic H_2O_2 synthesis (Eqs. 1–4). In this system, Mn(II) sites are oxidized to Mn(III) upon interaction with O_3, accompanied by the release of *OOOH species. The *OOOH species subsequently undergo spontaneous decomposition to generate hydroxyl radicals (•OH), which couple to form H_2O_2. Under light irradiation, photogenerated electrons facilitate the reduction of Mn(III) back to Mn(II), thereby completing the catalytic cycle. The efficiency of this cycle is governed by the utilization of photogenerated electrons, which play a critical role in regulating H_2O_2 production.

$$Mn(II)\cdots H_2O + O_3 \rightarrow Mn(III)\text{-}OH + {}^*OOOH \quad (1)$$

$${}^*OOOH \rightarrow {}^*OH + O_2 \quad (2)$$

$$2{}^*OH \rightarrow H_2O_2 \quad (3)$$

$$Mn(III) + e^- \rightarrow Mn(II) \quad (4)$$

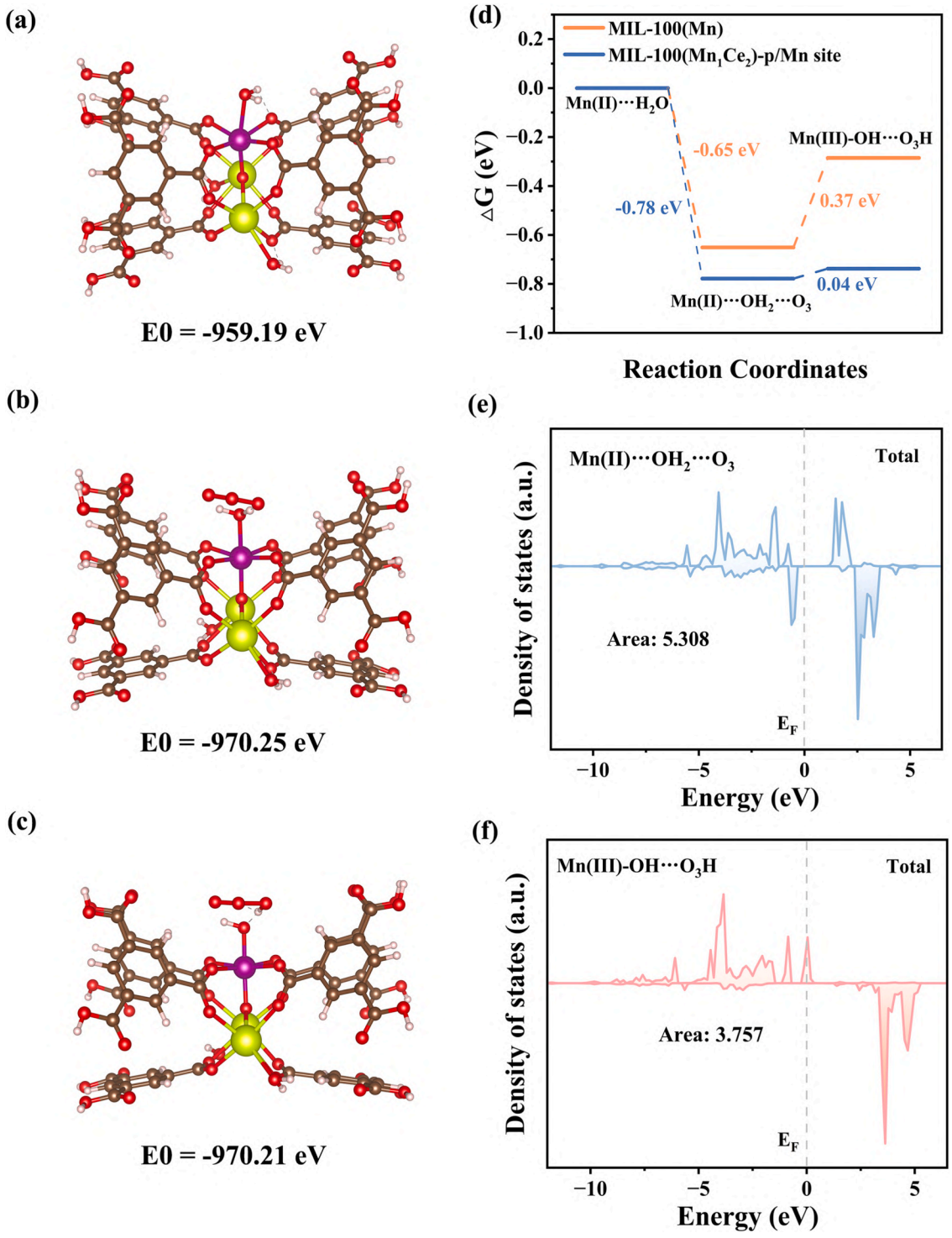

Fig. 5. (a-c) Adsorption energies of different structures of MIL-100(Mn_1Ce_2)-p/Mn site, **(d)** Reaction energy potentials at Mn sites of MIL-100(Mn) and MIL-100 (Mn_1Ce_2)-p/Mn site, The projected density of states (PDOS) of Mn in different intermediates **(e)** Mn(II)-OH_2···O_3 and **(f)** Mn(III)-OH···O_3H.

3.5. Theoretical calculation

Density functional theory (DFT) calculations were conducted to gain deeper insights into the reaction mechanism. Given that the catalytic reaction occurs in an aqueous environment, the initial structure was modeled as M···H_2O, where M represents the metal site. Taking MIL-100 (Mn_1Ce_2)-p/Mn site as an example, the sequential intermediates Mn (II)···H_2O, Mn(II)-OH_2···O_3 and Mn(III)-OH···O_3H are depicted in Fig. 5a-c. The corresponding structures for MIL-100(Mn) and the Ce site in MIL-100(Mn_1Ce_2)-p are shown in Figs. S9-S10. The associated energy profile indicates that the adsorption of O_3 on Mn(II)···H_2O is a highly exergonic process, suggesting strong thermodynamic spontaneity. Under the strong oxidizing environment of O_3, Mn(II) is oxidized to Mn (III), accompanied by hydrogen abstraction from O_3, forming Mn(III)-OH···O_3H. This step, involving an electron transfer process, is identified as the rate-determining step. The activation energy of MIL-100(Mn) is

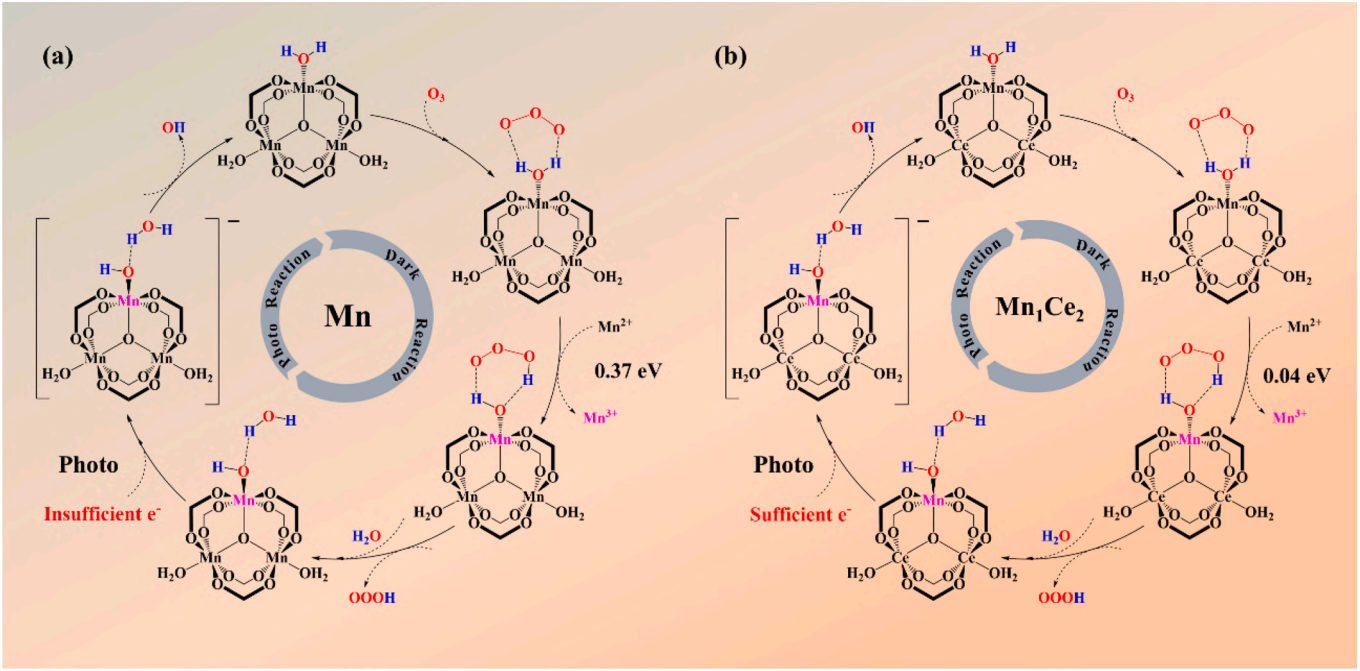

Schematic 2. Ozone-assisted photocatalytic mechanism for H_2O_2 synthesis over **(a)** MIL-100(Mn) and **(b)** MIL-100(Mn_1Ce_2)-p.

calculated to be 0.37 eV, whereas that of the MIL-100(Mn_1Ce_2)-p/Mn site is markedly reduced to 0.04 eV. The significantly lower energy barrier facilitates the generation of H_2O_2 in MIL-100(Mn_1Ce_2)-p. In contrast, the energy barrier of MIL-100(Mn_1Ce_2)-p/Ce site for the rate-determining step is 1.66 eV (Fig. S11), indicating that H_2O_2 formation primarily occurs at the MIL-100(Mn_1Ce_2)-p/Mn site.

The projected density of states (PDOS) was analyzed to investigate the electron transfer process during the interaction between O_3 and the Mn site in MIL-100(Mn_1Ce_2)-p. The PDOS diagrams for the s, p, and d orbitals of Mn(II)-OH_2···O_3 and Mn(III)-OH···O_3H are shown in Figs. S12-S17. The area below the Fermi level reflects the electronic distribution, where Mn(II)-OH_2···O_3 exhibits a significantly higher integrated PDOS value of 5.308, in contrast to 3.757 for Mn(III)-OH···O_3H. The observed reduction in electronic density at the Mn(III)-OH···O_3H site corresponds to an increased oxidation state of Mn, which is consistent with the XPS results. This correlation further substantiates the proposed reaction pathway.

In summary, the role of O_3 in the photocatalytic synthesis of H_2O_2 follows the pathway depicted in Schematic 2. Initially, Mn(II)···H_2O serves as the active site, where O_3 induces the oxidation of Mn(II) to Mn (III). Subsequently, the hydroperoxyl intermediate (*OOOH) is displaced by H_2O through solvation effects, forming a Mn(III)-OH···O_3H species. The incorporation of Ce reduces the activation energy of this rate-determining step from 0.37 eV to 0.04 eV. Under light irradiation, photogenerated electrons reduce Mn(III) back to Mn(II), regenerating the active site. The superior photogenerated electron utilization efficiency of MIL-100(Mn_1Ce_2) facilitates highly efficient catalytic cycling.

4. Conclusion

In summary, this study presents a groundbreaking ozone-coupled photocatalytic strategy for H_2O_2 synthesis using bimetallic MIL-100 (Mn_1Ce_2)-p, achieving an unprecedented yield of 1602 $\mu mol \cdot g^{-1} \cdot h^{-1}$ in pure water without the use of sacrificial agents, which represents a 240 % enhancement over monometallic analogs (e.g., MIL-100(Mn)). The system's exceptional stability (>50 h) and 83 % charge utilization efficiency stem from the synergistic Mn(II)/Ce(III) catalysis, where Ce doping optimizes the Mn-O-Ce charge-transfer pathway, reducing the energy barrier of the rate-determining step from 0.37 eV to 0.04 eV. Recent studies [39,40] on photocatalytic H_2O_2 production have exclusively focused on molecular oxygen (O_2) as the reactive oxidant; the present work establishes a new mechanism through experimental characterization and DFT calculations. O_3 adsorption on Mn(II)-H_2O sites triggers the oxidation of Mn(II) to Mn(III), followed by the solvation-induced removal of *OOOH and the formation of Mn(III)-OH···O_3H. Under light irradiation, photogenerated electrons efficiently reduce Mn(III) back to Mn(II), ensuring continuous H_2O_2 production. This mechanistic breakthrough paves the way for self-sustaining reactor systems to enable scalable and economical H_2O_2 synthesis.

CRediT authorship contribution statement

Guanqing Song: Writing – original draft, Investigation, Data curation, Conceptualization. **Chi Song:** Writing – original draft, Software, Data curation. **Gansheng Shi:** Software, Methodology, Formal analysis. **Xiao Wang:** Investigation, Formal analysis, Data curation. **Guanhong Lu:** Validation, Resources, Methodology. **Lu Chen:** Validation, Resources, Methodology. **Jing Sun:** Writing – review & editing, Supervision, Project administration. **Xiaofeng Xie:** Writing – review & editing, Supervision, Project administration, Conceptualization.

Declaration of competing interest

The authors declare that they have no known competing financial interests or personal relationships that could have appeared to influence the work reported in this paper.

Acknowledgment

This work was financially supported by the Jiangsu Key Laboratory of Coal-based Greenhouse Gas Control and Utilization (2025ZD01); Natural Science Foundation of Shanghai (22ZR1471800); China Postdoctoral Science Foundation (2023M740514); Basic and Applied Basic Research Foundation of Guangdong Province (2023A1515110680) and Hengdian Group Holding Co. LTD.

Appendix A. Supplementary data

Supplementary data to this article can be found online at https://doi.org/10.1016/j.jcis.2025.138801.

Data availability

Data will be made available on request.

References

[1] C. Xia, Y. Xia, P. Zhu, L. Fan, H. Wang, Direct electrosynthesis of pure aqueous H_2O_2 solutions up to 20% by weight using a solid electrolyte, Science 366 (6462) (2019) 226.

[2] Q. Wu, J. Cao, X. Wang, Y. Liu, Y. Zhao, H. Wang, Y. Liu, H. Huang, F. Liao, M. Shao, Z. Kang, A metal-free photocatalyst for highly efficient hydrogen peroxide photoproduction in real seawater, Nat. Commun. 12 (1) (2021) 483.

[3] R.J. Lewis, K. Ueura, X. Liu, Y. Fukuta, T.E. Davies, D.J. Morgan, L. Chen, J. Qi, J. Singleton, J.K. Edwards, S.J. Freakley, C.J. Kiely, Y. Yamamoto, G.J. Hutchings, Highly efficient catalytic production of oximes from ketones using in situ-generated H_2O_2, Science 376 (6593) (2022) 615.

[4] X. Zeng, Y. Liu, X. Hu, X. Zhang, Photoredox catalysis over semiconductors for light-driven hydrogen peroxide production, Green Chem. 23 (4) (2021) 1466–1494.

[5] Y. Fang, X. Wang, Peroxide production by porphyrins, Nat. Energy 8 (4) (2023) 325–326.

[6] Z. Yong, T. Ma, Solar-to-H_2O_2 catalyzed by covalent organic frameworks, Angew. Chem. Int. Ed. 62 (49) (2023) e202308980.

[7] H. Hou, X. Zeng, X. Zhang, Production of hydrogen peroxide by photocatalytic processes, Angew. Chem. Int. Ed. 59 (40) (2020) 17356–17376.

[8] J.D. Yang, X.K. Zeng, M. Tebyetekerwa, Z.Y. Wang, C.B. Bie, X. Sun, I. Marriam, X. W. Zhang, Engineering 2D photocatalysts for solar hydrogen peroxide production, Adv. Energy Mater. 14 (23) (2024) 2400740.

[9] X. Xiong, Z. Wang, Y. Zhang, Z. Li, R. Shi, T. Zhang, Wettability controlled photocatalytic reactive oxygen generation and Klebsiella pneumoniae inactivation over triphase systems, Appl Catal B 264 (2020) 118518.

[10] C. Kim, S.O. Park, S.K. Kwak, Z. Xia, G. Kim, L. Dai, Concurrent oxygen reduction and water oxidation at high ionic strength for scalable electrosynthesis of hydrogen peroxide, Nat. Commun. 14 (1) (2023) 5822.

[11] H. Li, Y. Li, X. Lv, C. Liu, N. Zhang, J. Zang, P. Yue, Y. Gao, C. Liu, Y. Li, A covalent organic framework as photocatalyst for smart conversion between photooxidation and photoreduction and H_2O_2 production in full pH environment, Adv. Mater. 37 (11) (2025) 2415126.

[12] D.K. Arriaga, A.A. Thomas, Capturing primary ozonides for a syn-dihydroxylation of olefins, Nat. Chem. 15 (9) (2023) 1262–1266.

[13] M. Coca, M. Peña, G. González, Kinetic study of ozonation of molasses fermentation wastewater, J. Hazard. Mater. 149 (2) (2007) 364–370.

[14] A. Gallo Jr., N.H. Musskopf, X. Liu, Z. Yang, J. Petry, P. Zhang, S. Thoroddsen, H. Im, H. Mishra, On the formation of hydrogen peroxide in water microdroplets, Chem. Sci. 13 (9) (2022) 2574–2583.

[15] S. Jodzis, T. Barczynski, Ozone synthesis and decomposition in oxygen-fed pulsed DBD system: effect of ozone concentration, Power Density, and Residence Time, Ozone: Science & Engineering 41 (1) (2019) 69–79.

[16] G. Song, C. Song, X. Wang, G. Shi, G. Lu, L. Chen, J. Sun, X. Xie, Construction of a novel MIL-100($Mn_{0.33}Er_{0.67}$) catalyst for efficient ozone removal over high humidity: unraveling the synergistic interaction between the transition metal and rare earth, Sep. Purif. Technol. 355 (2025) 129623.

[17] H. Reinsch, N. Stock, Formation and characterisation of Mn-MIL-100, CrystEngComm 15 (3) (2013) 544–550.

[18] J. Luo, H. Xu, Y. Liu, Y. Zhao, L.L. Daemen, C. Brown, T.V. Timofeeva, S. Ma, H. C. Zhou, Hydrogen adsorption in a highly stable porous rare-earth metal-organic framework: sorption properties and neutron diffraction studies, J. Am. Chem. Soc. 130 (30) (2008) 9626–9627.

[19] W. Li, X. Guo, P. Geng, M. Du, Q. Jing, X. Chen, G. Zhang, H. Li, Q. Xu, P. Braunstein, H. Pang, Rational Design and General Synthesis of Multimetallic Metal–Organic Framework Nano-Octahedra for Enhanced Li-S Battery, Adv. Mater. 33(45) (2021) 2105163.

[20] W. Guo, W. Xia, K. Cai, Y. Wu, B. Qiu, Z. Liang, C. Qu, R. Zou, Kinetic-controlled formation of bimetallic metal-organic framework hybrid structures, Small 13 (41) (2017) 1702049.

[21] Z. Wei, M. Liu, Z. Zhang, W. Yao, H. Tan, Y. Zhu, Efficient visible-light-driven selective oxygen reduction to hydrogen peroxide by oxygen-enriched graphitic carbon nitride polymers, Energ. Environ. Sci. 11 (9) (2018) 2581–2589.

[22] H. Shi, Y. Li, X. Wang, H. Yu, J. Yu, Selective modification of ultra-thin g-C_3N_4 nanosheets on the (110) facet of au/$BiVO_4$ for boosting photocatalytic H_2O_2 production, Appl Catal B 297 (2021) 120414.

[23] T. Liu, Z. Pan, J.J.M. Vequizo, K. Kato, B. Wu, A. Yamakata, K. Katayama, B. Chen, C. Chu, K. Domen, Overall photosynthesis of H_2O_2 by an inorganic semiconductor, Nat. Commun. 13 (1) (2022) 1034.

[24] B. He, Z. Wang, P. Xiao, T. Chen, J. Yu, L. Zhang, Cooperative coupling of H_2O_2 production and organic synthesis over a floatable polystyrene-sphere-supported TiO_2/Bi_2O_3 S-scheme photocatalyst, Adv. Mater. 34 (38) (2022) e2203225.

[25] Y. Teng, J. Zhao, Z.M. Ye, C.W. Tan, L.L. Ning, Y.Y. Zhou, Z. Wu, D.B. Kuang, Y. Li, Covalent organic framework encapsulating layered oxide perovskite for efficient photosynthesis of H_2O_2, Adv. Energy Mater. 15 (2024) 2404029.

[26] J. Sun, H. Sekhar Jena, C. Krishnaraj, K. Singh Rawat, S. Abednatanzi, J. Chakraborty, A. Laemont, W. Liu, H. Chen, Y.Y. Liu, K. Leus, H. Vrielinck, V. Van Speybroeck, P., Van Der Voort, pyrene-based covalent organic frameworks for photocatalytic hydrogen peroxide production, Angew. Chem. Int. Ed. 62 (19) (2023) e202216719.

[27] W. Zhao, P. Yan, B. Li, M. Bahri, L. Liu, X. Zhou, R. Clowes, N.D. Browning, Y. Wu, J.W. Ward, A.I. Cooper, Accelerated synthesis and discovery of covalent organic framework photocatalysts for hydrogen peroxide production, J. Am. Chem. Soc. 144 (22) (2022) 9902–9909.

[28] S. Liu, C. Zhu, J. Xu, L. Lu, Q. Fang, C. Xu, Y. Zheng, S. Song, Y. Shen, Efficient dual-pathway H_2O_2 production promoted by covalent triazine frameworks with integrated dual active sites, Appl Catal B 344 (2024) 123629.

[29] F. Liu, P. Zhou, Y. Hou, H. Tan, Y. Liang, J. Liang, Q. Zhang, S. Guo, M. Tong, J. Ni, Covalent organic frameworks for direct photosynthesis of hydrogen peroxide from water, air and sunlight, Nat. Commun. 14 (1) (2023) 4344.

[30] Y. Kondo, K. Honda, Y. Kuwahara, K. Mori, H. Kobayashi, H. Yamashita, Boosting photocatalytic hydrogen peroxide production from oxygen and water using a hafnium-based metal-organic framework with missing-linker defects and nickel single atoms, ACS Catal. 12 (24) (2022) 14825–14835.

[31] C. Feng, J. Alharbi, M. Hu, S. Zuo, J. Luo, H.S.A. Qahtani, M. Rueping, K.W. Huang, H. Zhang, Ultrafast charge transfer on Ru-cu atomic units for enhanced photocatalytic H_2O_2 production, Adv. Mater. 37 (12) (2025) 2406748.

[32] R.Q. Xia, Z.N. Liu, Y.Y. Tang, X. Luo, R.J. Wei, T. Wu, G.H. Ning, D. Li, A cyclic trinuclear silver complex for photosynthesis of hydrogen peroxide, Chem. Sci. 15 (35) (2024) 14513–14520.

[33] Y.-Y. Tang, X. Luo, R.-Q. Xia, J. Luo, S.-K. Peng, Z.-N. Liu, Q. Gao, M. Xie, R.-J. Wei, G.-H. Ning, D. Li, Molecular engineering of metal-organic frameworks for boosting photocatalytic hydrogen peroxide production, Angew. Chem. Int. Ed. 63 (36) (2024) 202408186.

[34] M.A. Mehrgardi, M. Mofidfar, R.N. Zare, Sprayed water microdroplets are able to generate hydrogen peroxide spontaneously, J. Am. Chem. Soc. 144 (17) (2022) 7606–7609.

[35] J. Cerkovnik, B. Plesničar, Recent advances in the chemistry of hydrogen trioxide (HOOOH), Chem. Rev. 113 (10) (2013) 7930–7951.

[36] Z.B. Sun, Y.N. Si, S.N. Zhao, Q.Y. Wang, S.Q. Zang, Ozone decomposition by a manganese-organic framework over the entire humidity range, J. Am. Chem. Soc. 143 (13) (2021) 5150–5157.

[37] L. Zhang, J.W. Yang, A.Q. Wang, S.H. Chai, J. Guan, L.F. Nie, G.J. Fan, N. Han, Y. F. Chen, High performance ozone decomposition spinel $(Mn,Co)_3O_4$ catalyst accelerating the rate-determining step, Appl Catal B 303 (2022) 120927.

[38] J. He, Y. Xu, P. Shao, L. Yang, Y. Sun, Y. Yang, F. Cui, W. Wang, Modulation of coordinative unsaturation degree and valence state for cerium-based adsorbent to boost phosphate adsorption, Chem. Eng. J. 394 (2020) 124912.

[39] G. Li, Q. Zhong, W. Wu, Y. Liu, H. Li, X. Li, T. Long, Effect of rare earth cerium doping on the activity of ZnO nanomaterials for producing H_2O_2 by piezoelectric catalysis, J. Colloid Interface Sci. 700 (1) (2025) 138431.

[40] M. Gao, J. Wang, Q. Chu, M. Meng, M. Xu, Y. Gong, Z. Zhang, Y. Cui, X. Wang, Y. Feng, C. Sun, Anthraquinone-functionalized bi-based metal-organic frameworks/BiOCl S-scheme heterostructure with enhanced interfacial electric field for efficient H_2O_2 production, J. Colloid Interface Sci. 698 (2025) 138099.